Thermal model for the directed energy deposition of composite coatings of 316L stainless steel enriched with tungsten carbides

Seifallah Fetni [a,*], Tommaso Maurizi Enrici [b], Tobia Niccolini [a], Hoang Son Tran [a], Olivier Dedry [b], Laurent Duchêne [a], Anne Mertens [b], Anne Marie Habraken [a]

[a] University of Liège, UEE Research Unit, MSM division, allée de la Découverte, 9 B52/3, B 4000 Liège, Belgium
[b] University of Liège, Aerospace & Mechanics, MMS Unit, allée de la Découverte, 9 B52/3, B 4000 Liège, Belgium

HIGHLIGHTS

- A thermal model for the Directed Energy Deposition of a novel composite coatingis presented.
- The conducted analyzes explain the dissolution of carbides and the formation of a carbon network around the grains.
- Thermo-physical properties of a new Metallic Composite Material are here presented.
- This work presents an exhaustive explanation of the methodology of calibration of 2D models for additive manufacturing.

GRAPHICAL ABSTRACT
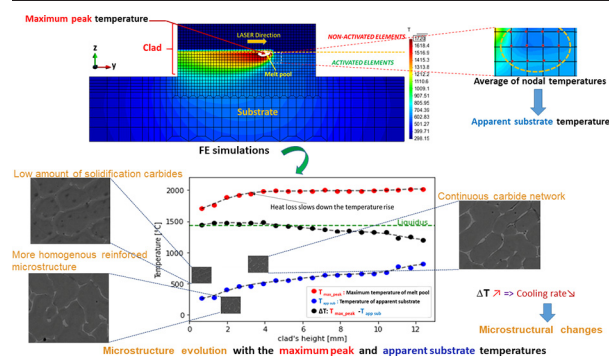
ARTICLE INFO

ABSTRACT

This work focuses on the thermal modeling of the Directed Energy Deposition of a composite coating (316L stainless steel reinforced by Tungsten carbides) on a 316L substrate. The developed finite element model predicts the thermal history and the melt pool dimension evolution in the middle section of the clad during deposition. Numerical results were correlated with experimental analysis (light optical and scanning electron microscopies and thermocouple records) to validate the model and discuss the possible solidification mechanisms. It was proven that implementation of forced convection in the boundary conditions was of great importance to ensure equilibrium between input energy and heat losses. The maximum peak temperature shows a slight increase trend for the first few layers, followed by an apparent stabilization with increasing clad height. That demonstrates the high heat loss through boundaries. While in literature, most of the modeling studies are focused on single or few layer geometries, this work describes a multi-layered model able to predict the thermal field history during deposition and give consistent data about the new materiel. The model can be applied on other shapes under recalibration. The methodology of calibration is detailed as well as the sensitivity analysis to input parameters.

1. Introduction

Directed Energy Deposition (DED) has become an attractive technique for manufacturing thanks to different promising features: fine grain size, low dilution and good mechanical properties. The control of the output microstructures has been a serious challenge, the goal is to obtain built-samples with optimized qualities, in order to be applied in advanced and critical conditions: aerospace, medical…industries. [1–4].

316L Stainless Steel (SS) is a good candidate for various Additive Manufacturing (AM) techniques: Selective Laser Melting (SLM) [5,6], Laser Powder Bed Fusion technologies (L-PBF), DED [7], Laser Engineered Net Shaping (LENS) [8,9] etc. However, some limitations

have been reported. In fact, although SS means improved corrosion resistance, associated low hardness as well as the tendency to scoring make it vulnerable to wear [10].

Strengthening the 316L metallic matrix with strong phases (e.g. carbides [11] or nanoparticles addition [12,13]) is a promising alternative in DED process allowing the manufacturing of metal matrix composite coating. Enrichment of 316L SS by tungsten carbide (WC) leads to improve the associated mechanical properties, in particular surface hardness and wear resistance. Indeed, WC carbides permit to retain room temperature hardness of the composite coating up to 1400 °C [14]. AM processes, in particular DED, are principally characterized by a dynamic and localized laser energy input able to completely or partially melt the amount of powder involved, depending on the melting temperature of the materials and the process parameters. These specific manufacturing conditions generate out-of-equilibrium phases formed by partially dissolved carbides within the liquid phase and extreme cooling rates. As a consequence, the sample characterization reveals a microstructure which is not reproducible through traditional manufacturing techniques [11].

Due to high manufacturing costs and non-negligible time for trials and errors, numerical simulations are adequate tools to optimize the process parameters before building samples. Currently, numerical tools are able to predict some important data such as thermal history and melt pool dimensions and to tackle microstructure complexity. Indeed, the thermal field and its history give a better understanding of the chemical and thermo-physical phenomena occurring during the process. Several 2D and 3D models have been developed to predict geometry [15,16], formed microstructure [17], mechanical properties [18] as well as solidification kinetics [1,19,20] etc. In particular, several 3D models using Finite Element Method (FEM) for simulation of DED processes exist in the literature. Zhang et al. [21] developed a 3D thermal finite element model in order to study the heat transfer during DED of 420 SS + 4% of molybdenum on a mild steel A36. They found a good correlation in geometric predictions compared to experimentation. Within their thermal model, local convection due to fluid motion (thermo-capillary induced Marangoni flow) was considered by modifying the thermal conductivity. They added an adjusted multiplicative coefficient in the modeling of the thermal conductivity when temperature was above melting point. They found that the microstructure of the clad parts changed from a cellular morphology to a columnar one and presented finer dendrites going from the bottom to the top surface of the clad. Knapp et al. [22] developed a 3D model for a single pass AM deposition, applied on stainless steel 316L and Alloy 800H in order to estimate geometry (curved surfaces), transient temperature, cooling rates, velocity distribution as well as solidification mechanisms (secondary dendrite arm spacing). These authors mentioned that acceptable predictions of clad properties were obtained by some previous studies which neglected the effects of convective flow of molten metal inside the pool during the computation of temperature distributions [2,3,23]. However, they found that the convective flow driven by Marangoni effect changes the temperature distribution, the cooling rates and the solidification morphology [22]. In the same way, Svensson et al. [24] showed that only considering heat conduction is an over simplifying assumption for an accurate prediction of temperature gradients and heat flux inside the melt pool.

The main limitation of 3D FEM models is that they require long computation time even with simplifying hypotheses. In this respect, most of the detailed developed models focused on single or few layer geometries. However, global temperature increases with built height [25]. As a result, when the clad height increases, the microstructure is coarsened due the decrease of the cooling rates. Therefore, focusing on the implementation and applicability of 2D models is of great interest. However, as the third dimension is lost, some assumptions have to be added for the out of plane behavior. It is also necessary to adapt within the model some input parameters such as the laser power, idle time, process speed, substrate geometry…to compensate the planar modeling assumption [26,27]. Even if 2D FE models cannot predict results in the third direction, their computed evolution of the melt pool depth, as well as the thermal history, is useful to adjust the processing parameters before cladding. Ya et al. [28] proposed a 2D thermal model for DED process based on mass and energy balance in order to accurately predict the clad geometry and the temperature cycles when depositing one layer composed of 11 overlapped clad tracks. Computed melt pool and Heat Affected Zone (HAZ) dimensions were compared to experimental results, and good agreement was reported. However, fluid convection was neglected. Parekh et al. [29] took into account thermo-capillary forces when they developed a 2D model using Comsol multi-physics software. They aimed to study the influence of processing parameters on the clad geometry. Cited works gives consistent results for the prediction of the deposited one-layer geometries. Nevertheless, multilayered components is still a major challenge whether in 2D or 3D modeling.

A calibrated 2D model can help to understand the microstructure genesis through the computed thermal history of material points [26]. However, great attention must be paid to thermo-physical properties (thermal conductivity, specific heat capacity and density) of the clad material. Indeed, these properties must be measured on the clad and not on samples produced by other processes. Otherwise, as reported in [30,31], some discrepancies in the simulation results are expected. Any numerical model has to be validated against experimental results and different measurement techniques can be used: thermocouple records, optical micrographs, micro-hardness measurements, high speed imaging etc. As done in most recent numerical studies focusing on additive manufacturing [21,32–34], a double validation of the models (by the mean of two techniques or more) is required in order to enhance the confidence about the finite element results before their application on real processes.

Additionally, during DED modeling, thermal boundary conditions, namely convection and radiation, must be duly considered. These physical phenomena, in particular convection, were not taken in account or neglected in some works [35,36] or assumed uniformly distributed over the external surfaces, e.g. free convection ($\approx$ 1–10 W/m^{2}K) [37–39]. In recent works, the fundamental role of heat convection in the energy balance during AM processes was highlighted. The amount of heat transferred by convection and radiation increases with the processing time as a result of natural conditions or the inert gas jets flowing along the increasing external surface of the deposit. Gouge et al. [40] concluded that using free convection alone is better than ignoring convective heat losses, but it could not give a reliable prediction of the thermal field. Heigel et al. [41] were the first to develop a measurement-based forced convection model.

A first approach about the implementation of a 2D thermal model to simulate the DED manufacturing of composite coatings in 316L SS with WC is available in [42]. However, the experimental validation was not achieved. In the present work, input parameters of the model are adjusted in order to obtain a reliable prediction of both the thermal history and the melt pool depth. Improved assumptions are also implemented. Appropriate boundary conditions are applied such as forced convection for instance convective flow in the liquid phase. An exhaustive description of the model calibration methodology is presented. The validated model is then used to analyze the thermal field evolution, in particular the heat accumulation phenomenon and its impact on final microstructures. An emphasize is put on the maximum peak temperature as well as the apparent substrate temperature. These temperatures generated by the validated model provide interesting explanations of the microstructure evolution during deposition.

2. DED experimental process

2.1. Laser cladding parameters

A 5-axis Irepa Laser Cladding (LC) system with a Nd-YAG laser source was used to melt the mixture of 316L SS+ WC powders on the substrate of 316L SS as illustrated in Fig. 1. The substrate was fixed on the machine by concentric clamping (3 clamping jaws). The dimensions of the manufactured sample are shown in Fig. 1b. The main process parameters are gathered in Table 1. Globally, the powders presented a spherical shape and a granulometry distribution ranging from 50 to 200 μm [11]. Such a shape reduces the scattering effect of the laser beam which makes it more concentrated on the clad area and limits the energy loss. Laser scattering as well as laser light diffraction are some typical examples of laser power ineffectiveness [43,44]. After placing the two powders inside the tanks, a few hours delay is applied before starting the process in order to let the powders set. Then, the two powders can be dragged separately, through an inert gas flow from their respective storage tank to the nozzle. The deposition was performed with a powder direction between 38 and 45°. Another important parameter to set is the distance between the nozzle and substrate. Indeed, on the one hand, if this distance is too large, there is a risk of excessive dispersion of energy before deposition. On the other hand, a too small distance does not ensure a sufficient laser footprint area for the creation of a proper molten pool geometry. The optimum
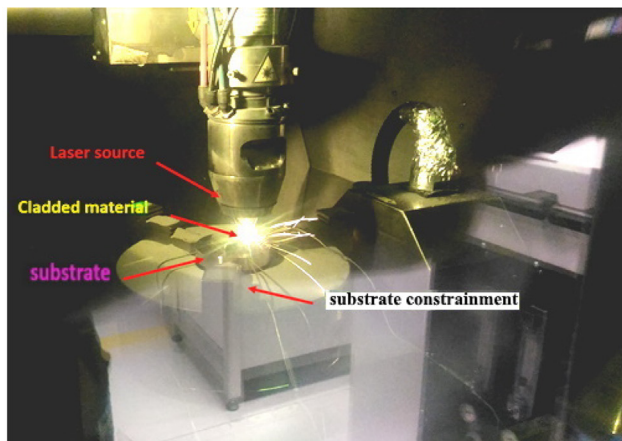
(a)
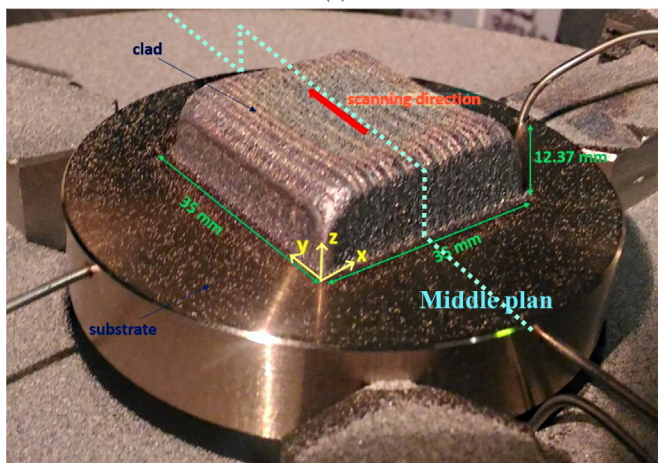
(b)

Fig. 1. A real view of the Irepa 5-axis laser cladding machine (a) and a zoom on the manufactured sample (b).

Table 1
Process parameters of sample manufacturing by Irepa machine.

Laser Power (W)	Laser diameter (mm)	Scanning speed (mm/min)	Powder flow (g/min)
570	1.5	290	23.4

distance of 10 mm between the laser nozzle and the substrate was selected after several deposition tests. The complete or partial melting of the powder principally depends on its melting temperature, but also on the powder size and on the laser transverse speed and power. The final sizes of the samples are $35 \times 35 \times 12.3$ mm. These dimensions as well as the positions of the different thermocouples are illustrated in Fig. 2.

The deposition is based on cycles of four layers described in Fig. 3. The samples were made up by 19 superimposed layers consisting in four complete cycles (16 layers) and three additional layers (the deposition stops at End3 point in Fig. 3). A shift of half a track width was introduced in order to obtain a good overlapping of two consecutive layers.

2.2. Thermocouple records

Among the four thermocouples, T3, the one located just below the clad, was selected for the model identification (see Fig. 2a). In T3 temperature-time curve (Fig. 4), each wave corresponds to one layer and contains 26 'sub peaks' associated with each track. Within the 2D modeling, the different tracks cannot be explicitly considered. Therefore, the analysis of the experimental temperature curve is focused on the 13*th* track of each layer. This track is in the middle of each layer and corresponds the passage of the laser just above the thermocouple T3. The minimum and maximum temperatures at T3 during the 13*th* track or adjacent to this track (highlighted by the three red dots in Fig. 4) are experimental targets for the 2D model. The maximum temperature during the 13*th* track is also the maximum temperature achieved during the current layer. The total deposition time is about 4000 s. However, the total simulation time needs to be scaled for the 2D modeling. The scaling is based on the 3 fundamental temperatures associated to the 13*th* track to define the reference experimental curve of the 2D model (red points in Fig. 4). They represent the temperature evolution for the 2D model and they are used as references to set the duration of the 2D thermal simulation. In addition, average heating and cooling periods (defining a numerical idle time), associated with the tracks 1 to 12 and 14 to 26 respectively, are added in the 2D model in order to accurately model the 3D process.

2.3. Determination of the real melt pool depth

A new investigation technique was developed to estimate the melt pool depth at the moment of its deposition. A low optical magnification (LOM) of the clad zone at the end of the process is illustrated in Fig. 5, while a higher magnification is shown in Fig. 6. The first circle in cyan (Surface 1) was drawn by enclosing the lower edge of the experimental melt pool which is highlighted by the dashed yellow curves. The microscope tools are able to automatically provide the area of the circle. Then, the second circle in red (Surface 2) was drawn for the same track. The reference points for the second circles are also based on the boundaries between the tracks at the end of the process: the highest point of the track and the lowest one, where a tangency condition between the first and the second circle is added. In this way, two limits are defined for the melt pool size: an upper limit defined by D_1 (diameter of Surface 1) and a lower one by D_2 (diameter of Surface 2). This operation is repeated taking into account 5 medium tracks per layer (tracks 11 to 15). The result average and its variance are shown in Fig. 7 expressing the experimental melt pool depth. For both D_1 and D_2 diameters, a
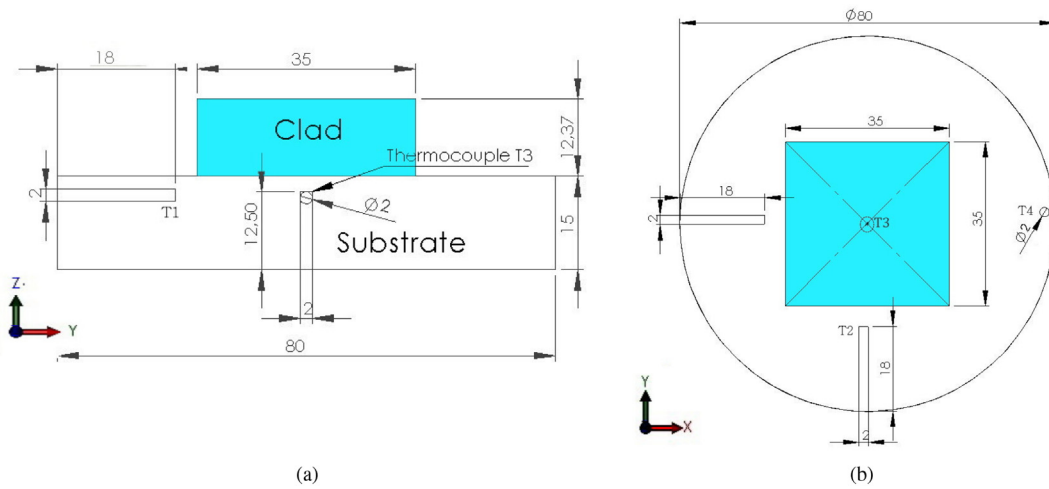
Fig. 2. YZ (a) and XY (b) views of the manufactured sample as well as the positions of the different thermocouples.

constant trend can be observed except for the first and last layers. For the initial layer, a big dispersion of values of diameters D_1 and D_2 is observed. Indeed, at the beginning of the deposition, the powders output may slightly vary until a steady condition. For the last layer, the D_2 diameter is higher compared to its previous value. This last measurement is explained by the absence of remelting by the next layer. For other layers, a partial remelting occurs for each layer by the subsequent one. Some material is then transferred to the next layer. The D_2 value and specifically the last layer value is expected to be the closest information about the actual value of the melt pool depth. D_1 always overestimates the melt pool size (it is an upper limit). The computed melt pool depth (noted MP_{FEM}) should remain between D_1 and D_2. Indeed, the numerical melt pool depth is computed at the moment of deposition while the diameters D_1 and D_2 are measured after the deposition of all the layers. The remelting effect by the next layer should be considered. Thus, in order to roughly estimate a target value of the melt pool depth, D_2 is multiplied by a η coefficient which represents the ratio between the height of the last layer (number 19) and the average value of the previous layers (except the first one). Hereafter, the value $D_2^*=\eta$. average(D_2) is chosen as the experimental melt pool depth during the

deposition process (green doted line in Fig. 7b). The value of 1.23 was found for the coefficient η. The corrected diameters D_2^* are also shown in Fig. 7b. A constant melt pool depth is a reasonable assumption based on the low variations of D_1 and D_2 (Fig. 7) and microstructural analyzes of carbide dissolution within the recent experimental analysis of 316L SS+ WC powder processed by DED [11].

3. Thermo-physical properties of materials

The solidus and liquidus values of composite coating are reminded in Table 2. The thermo-physical properties of 316L are available in literature [45–51]. Additionally, the thermophysical properties of the 316L substrate were measured by the same procedure as described below for the SS 316L + WC composite. In order to consider as much information as possible concerning the thermal conductivity and specific heat capacity of the substrate, literature data were collected, then a linear fitting was done. The obtained temperature-dependent relationship was implemented in the numerical model. In this way, a better connection with the physical reality of heat transfer phenomena is ensured and reliable input data is achieved. Collected data about 316L SS specific heat capacity and thermal conductivity are gathered in Fig. 8.

Thermo-physical properties of the composite coating were measured in Uliège by MMS laboratory. After deposition, the sample was carefully cut in the middle, in order to obtain cylinders of 5 mm of diameter for sample. The differential scanning calorimetry (DSC) technique was used to measure the specific heat capacity with the DSC 404C from Netzsch. A dilatometry test was performed to measure the sample linear dilatation (DIL 402C apparatus from Netzsch). Change in length was measured according to standard DIN 51045. The room temperature density was determined by combining a measurement of the mass of the sample using a high precision weighing scale (0.1 mg) and a measurement of the volume of the same sample using an Accupyc 1340 Helium pycnometer from Micromeritics. Thermal diffusivity was measured by Laser Flash method using a Netzsch LFA 427 apparatus. Finally, the thermal conductivity was calculated using the parameters previously determined by dilatometry, DSC and laser flash diffusivimetry according to the relationship: $k(T) = \alpha(T). \rho(T). C_p(T)$; where k is the thermal conductivity (W/m.K), α the thermal expansion coefficient in K^{-1}, ρ the density in kg.m^{-3} and C_p the specific heat capacity in J/kg. K. Experimental results are presented in Fig. 9. It can be observed that, by adding 20%wt of WC to the 316L matrix, the thermal conductivity is enhanced. The drop in thermal conductivity and specific heat capacity near 1000 K can be explained by the dissolution of secondary carbides.
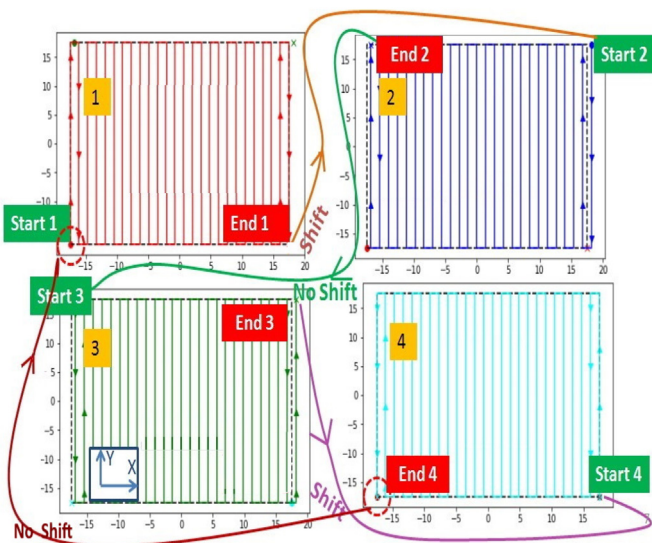

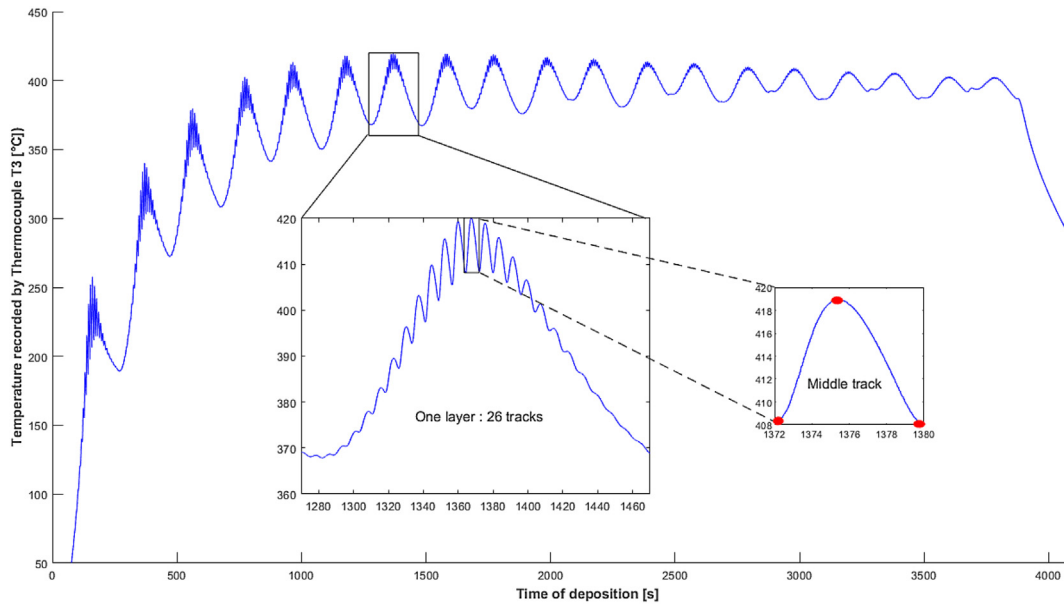**Fig. 3.** Laser path of the DED process.

Fig. 4. Temperature evolution at thermocouple T3 during deposition.

4. Numerical model

4.1. Mesh characteristics and software presentation

The thermal field is computed using the finite element (FE) software Lagamine developed at the University of Liège. This implicit FE code was validated by measurements [52] and benchmarks [53]. Within this study, the BLZ2T thermo-mechanical solid finite element is selected. Only associated thermal degrees of freedom are activated.

The top surface elements of the clad are subjected to the laser heat source. For this reason, a refinement was chosen within the clad. The element size is related to the heat source laser diameter [54]. In order to reduce the simulation time, a coarser mesh was drawn in the substrate. Meanwhile, to ensure a good link between the clad and the substrate as well as the position of the thermocouple, the mesh is refined which also avoids numerical temperature fluctuation due to very high temperature gradient. Convection and radiation interface elements (called hereafter ConRa elements) surround the whole model, this configuration is very similar to the experimental set-up. It should be reminded that the bottom part of the substrate is also subjected to convection and radiation because it is a free surface, however the dimensions of the clamping joints are neglected. The mesh is shown in Fig. 10.

4.2. Heat transfer equations and input of laser power

The temperature distribution (T) in the clad and substrate (316L) was computed based on the classical formulation of heat transfer:

$$k\left(\frac{\partial^2 T}{\partial x^2} + \frac{\partial^2 T}{\partial y^2} + \frac{\partial^2 T}{\partial z^2}\right) + Q_{int} = \rho C_p \frac{\partial T}{\partial t} \tag{1}$$

here Q_{int} (W/m^3) is the density of the power generated in the workpiece.

The surface heat exchange by convection and radiation was defined by the following equation:

$$-k\left(\frac{\partial T}{\partial x}\right) = -h(T-T_a) - \varepsilon\sigma\left(T^4 - T_a^4\right) - Q_r \tag{2}$$

where h is the convective heat transfer coefficient in W/m^{2}K. T_a the room temperature, ε the emissivity coefficient, σ the Stefan-Boltzmann constant (W/m^{2}K^4). Q_r is the laser heat flux expressed as:

$$Q_r = \beta\frac{2P}{\pi r_L^2} \tag{3}$$

here β is the absorption factor, P the laser power and r_L the laser beam radius. This coefficient loses its physical meaning in 2D modeling which neglects the heat flow in the orthogonal direction of the 2D mesh. It was fitted by comparing the experimental and numerical temperature-time curves of substrate temperature (Thermocouple T3 records). The laser power is simply expressed by:

$$Q_{2D} = \beta_{2D}.P \tag{4}$$

where β_{2D} takes into account the section assumed by the software as well as the absorption fraction of the energy. This laser heat flux is applied on 3 adjacent nodes. In the numerical tool, the birth and death technique was adopted and is illustrated in Fig. 11.

4.3. Specific assumptions in 2D FE model

To conduct this work, some assumptions are taken into account and detailed as follows. First, the 13*th* track, which corresponds to the laser path in the middle of one layer deposition, is the one considered for the 2D FE model. The middle plane has indeed a representative microstructure of the sample not affected by edges. The real scanning speed is kept in the numerical model to better mimic the reality as well as the thermo-physical properties and the geometry. Meanwhile, the influence of the 25 other tracks within each layer as well as the out of plane thermal flow have to be compensated by adjusted boundary conditions (convection, radiation and idle time). Indeed, in a 2D model, because of this out of plane missing flow and global cooling of the whole sample (see Fig. 1), the physical meaning of the absorption coefficient β of the laser power is lost. Heat convection and radiation emissivity
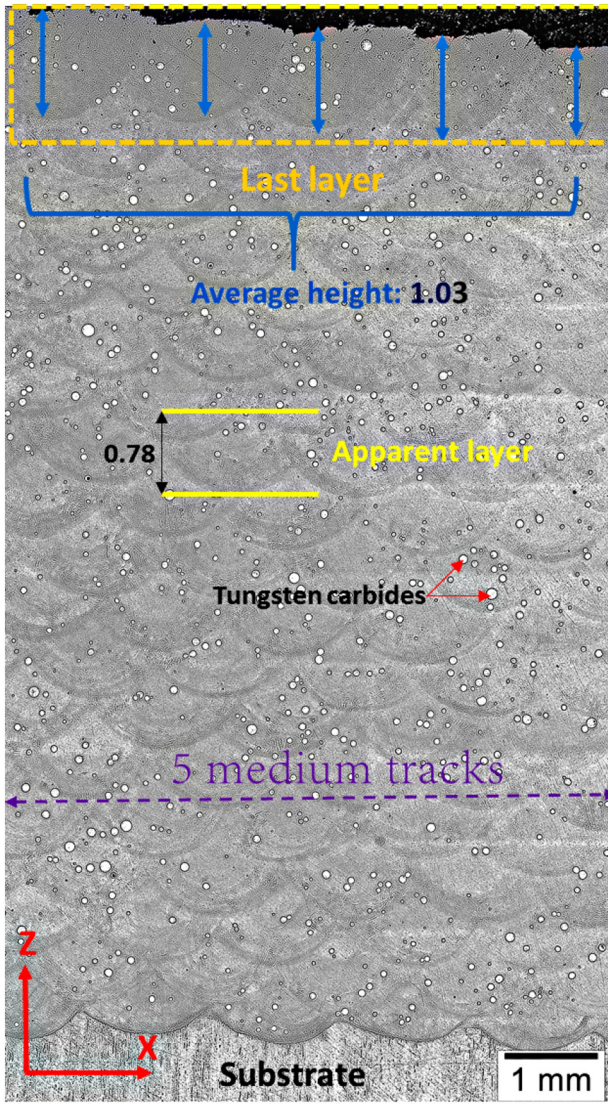
Fig. 5. LOM image illustrating the 5 medium tracks for each of the 19 subsequent layers of the clad.

coefficients are adjusted by inverse modeling. Another impact of the 2D FE model is the real process time scaling in order to compare the scaled thermocouple curve to the computing one. The whole temperature
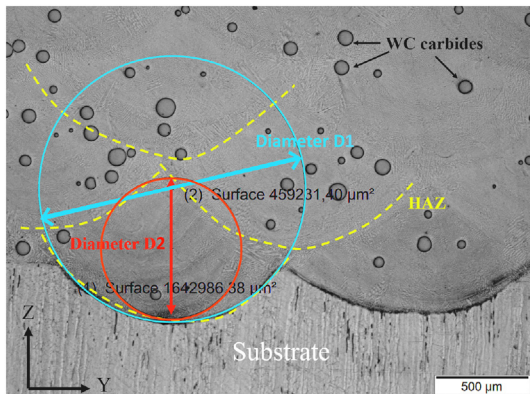

Fig. 6. Definition of the limits of the molten pool.

evolution is scaled in virtual time axis (time required for the 13*th* deposition with the correct laser velocity and virtual idle time). Finally, most of the heat input will be transferred by conduction to the substrate. As the third dimension is not considered, the loss along the X direction (see Fig. 10) must be compensated by an appropriate coefficient of convection. This coefficient has to be high enough to ensure thermal equilibrium between energy absorption and heat loss. Therefore, the clad zone is considered to be in forced convection during DED in addition to thermal radiation. The range of the values of convective heat transfer coefficient is identified by inverse modeling.

It should be noted, that an additional assumption is considered but not limited to 2D modeling; the use of modified conductivity in thermal modeling to take in account fluid motion and Marangoni effect within the melt pool as mentioned in the introduction.
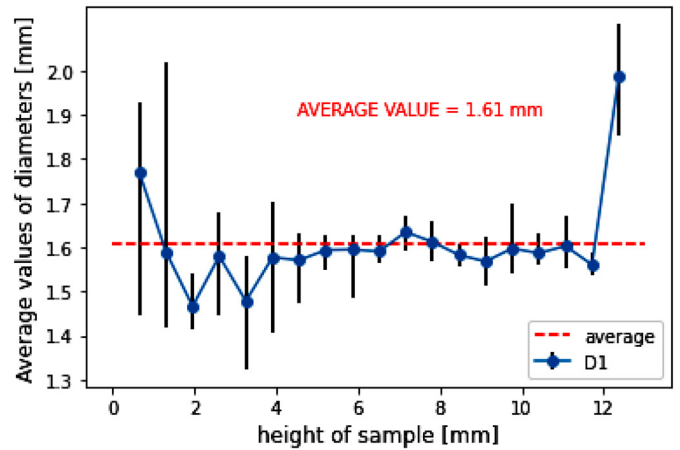
(a)
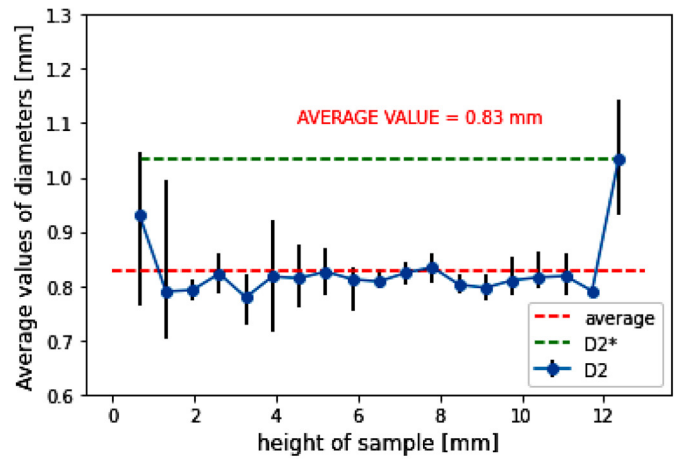
(b)

Fig. 7. Experimental results of melt pool measurement using two circles investigative technique.

Table 2
Liquidus and solidus temperature (°C) of the composite material [11].

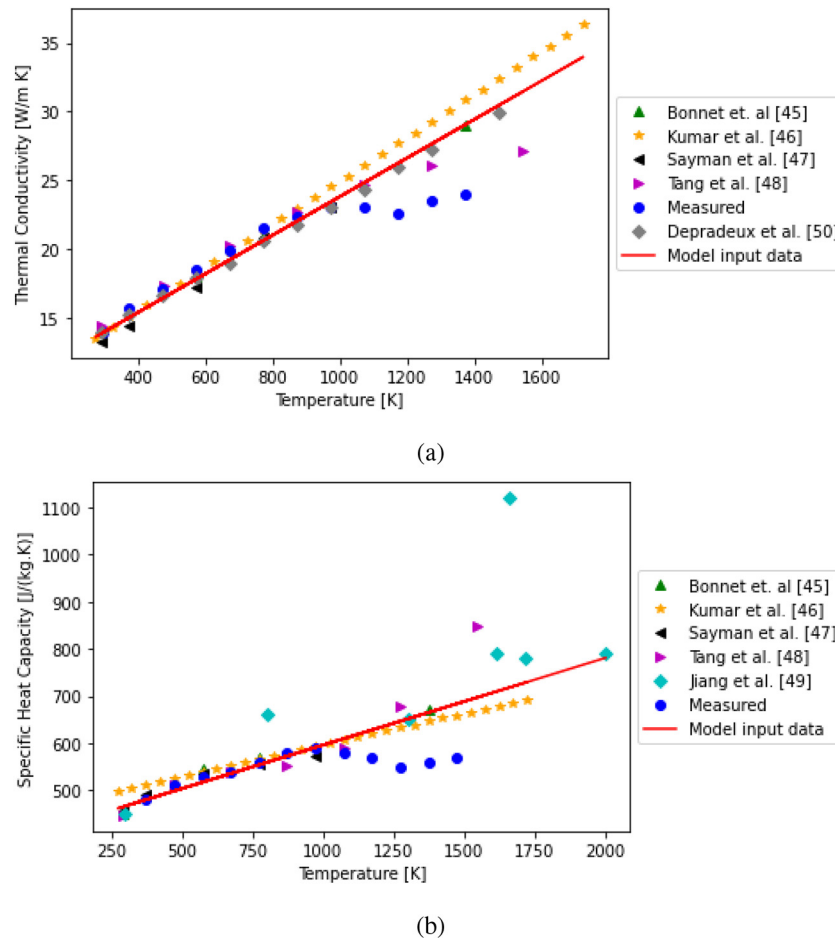| Property	Composite Coating
Liquidus Temperature [°C]	1450
Solidus Temperature [°C]	1354

(a)

(b)

Fig. 8. Gathered thermo-physical properties of 316L SS, (a): thermal conductivity [W/m.K] and specific heat capacity [J/Kg.K].

4.4. Clad subdivision

In order to ensure a better control of boundary conditions (convection and radiation), different sub-divisions of the clad are defined as shown in Fig. 12. The experimental measurements of Heigel et al. [41], have proven that the thermal convection and radiation coefficients increase their magnitude along the sample height. To give to the FE model the flexibility to simulate these boundaries conditions, the substrate is divided into different ConRa zones; the upper horizontal surface (called 'substrate top') and the edges: the bottom and vertical sides (simply called 'substrate'). The first zone receives more heat due to the direct exposition to laser heat and need to be associated to a forced convection regime as explained in the state of art [40,41]. This subdivision allows to define different values for convective heat transfer coefficient (h) and (if necessary) emissivity (ε) as a temperature function for each zone. Different boundary conditions for different clad layers are possible too. Commonly, the higher values of h are imposed to the initial layers (mainly layers 1, 2 and 3: bloc 1). In this region, the highest thermal gradients are achieved as no preheating of the substrate was applied. For upper blocs, a constant value is affected to all blocks in a first order. The accurate identification of convection value for each block is ensured by inverse modeling based on the constant melt pool size value and the thermal history.

## 5. Results and discussion

5.1. Sensitivity analysis

The 2D model calibration process is guided by the sensitivity of the temperature history at the thermocouple to different input parameters.

In a decreased impact ranking, one has: laser power P, idle time, convective heat transfer coefficient h and radiation ε, according to previous works on 2D modeling of DED process applied on M4 [26], 316L SS + WC [55] and Ti6Al4V [56] alloys. A modified conduction value of the clad is also chosen (increased value within the melt pool) and defined before the calibration process. The approach for the model calibration consists in testing sensitivity of the least influential parameters in the first step then the most influential ones. The logic of such a methodology is to find the best compromise between a general good trend of the computed thermocouple curve and the evolution of the melt pool depth. As laser power is the first parameter influencing the computed thermal field, it is easily defined on the first layers then adjusted at the end of the calibration process. The next step of the calibration is to test the sensitivity of the model to the convection and radiation. Finally, sensitivity to idle time variation is investigated in order to find the appropriate range of values ensuring a good energy balance and melt pool depth. Based on the experimental investigations (section 2.3), the melt pool depth has been found relatively constant during the whole deposition time. The objective is then to find the range of idle time values that ensures this trend. The final target is a set of parameters able to predict both the T3 temperature curve and the melt pool depth.

### 5.1.1. Sensitivity to modified conduction factor

For these simulations, the power input is defined by a β_{2D} coefficient of 0.24 (see eq. 4), while the idle time between layers is set to 2 s based on [26]. These values are selected as they give acceptable trend of the temperature curve at thermocouple T3 for the first layers. Predicted temperature distribution should consider the effects of convective flow inside the molten pool [22]. According to [57], ignoring these
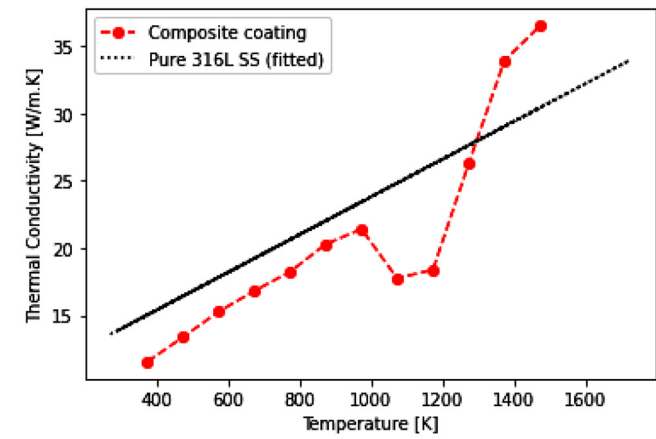
(a)
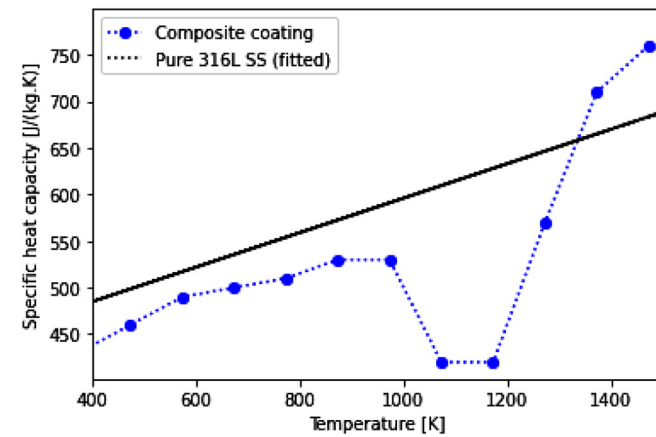
(b)
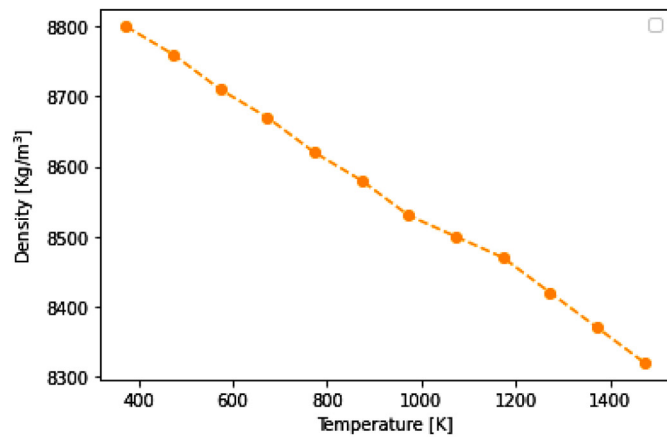
(c)

Fig. 9. Measured thermo-physical properties of the composite coating in function of temperature, (a) thermal conductivity [W/m.K], (b) specific heat capacity [J/Kg.K] and (c) density [Kg/m³].

Fig. 10. FE 2D mesh used to model the DED process as well as the boundary conditions surrounding the model.

Fig. 11. Activation element technique used to model DED.

Fig. 12. Different boundary conditions applied through different data set within ConRa interface element.
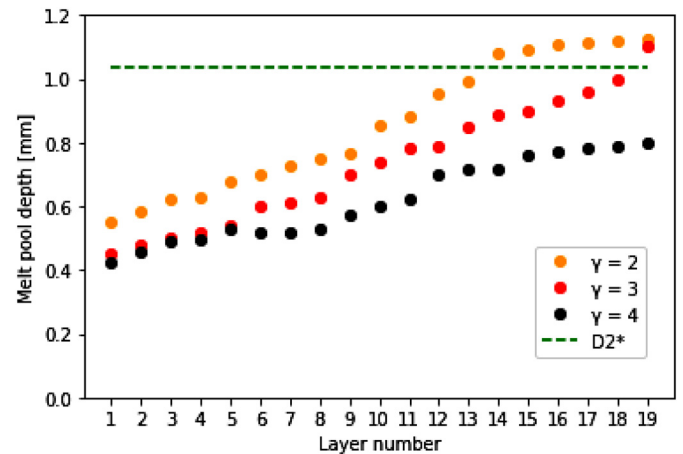
Fig. 13. Variation of predicted melt pool depth with clad height for different modified conductivities (γ coefficient).

effects lead to overestimate cooling rates. To model the Marangoni flow, the experimental conductivity above solidus temperature is multiplied by a coefficient γ to get a modified value $k^* = \gamma.k$. Hereafter, within FE model, γ value will be equal to 3 based on different trials (Fig. 13) and on some literature data ($\gamma = 2.5$ in [58], $\gamma = 5$ in [21]). It could be inferred that the higher is the conductivity, the lower is the melt pool depth. As heat transfer by conduction is increased, the melt pool size decreases as well as Marangoni effect. Selected value provides a compromise
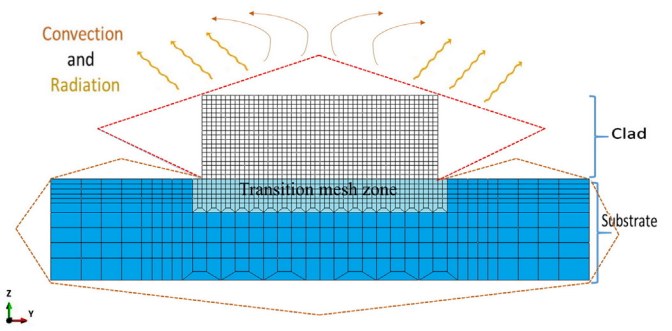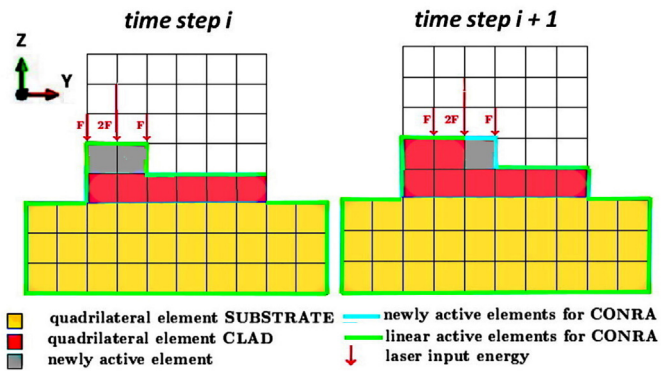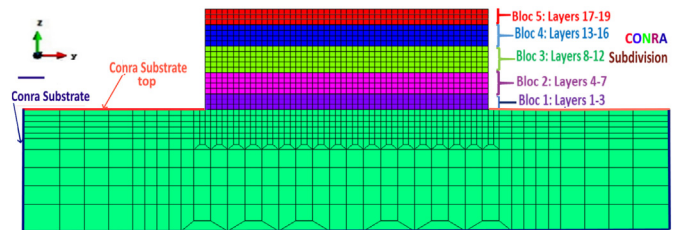
Table 3
Convection and emissivity values chosen to test the sensitivity of the model.

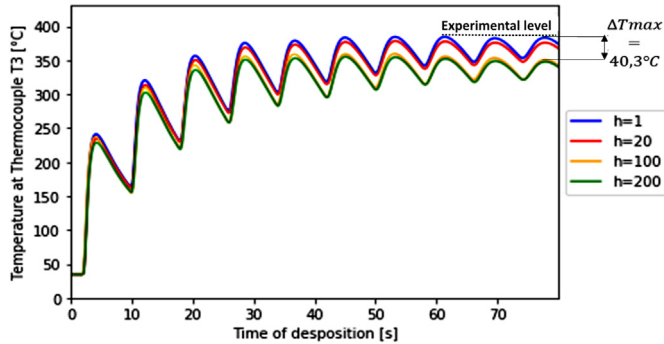|	Set 1				Set 2			
h_{Clad} [W/m²K]	1	20	100	200	10			
ε_{Clad}	0.8				1	0.8	0.4	0.1
$h_{substrate}$ [W/m²K]	2500				2500			
$\varepsilon_{substrate}$	0.8				0.8			

Fig. 14. Sensitivity analysis: variation of the coefficient h (data set 1).
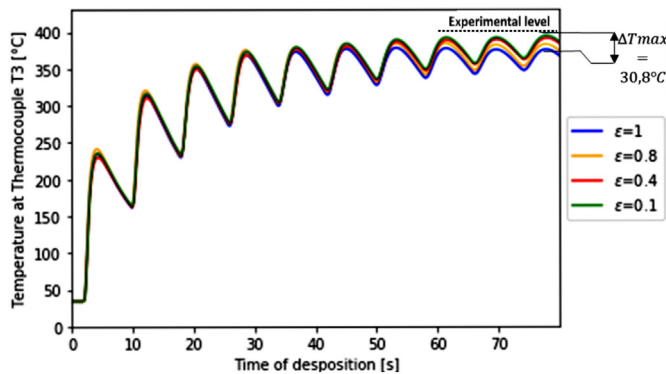
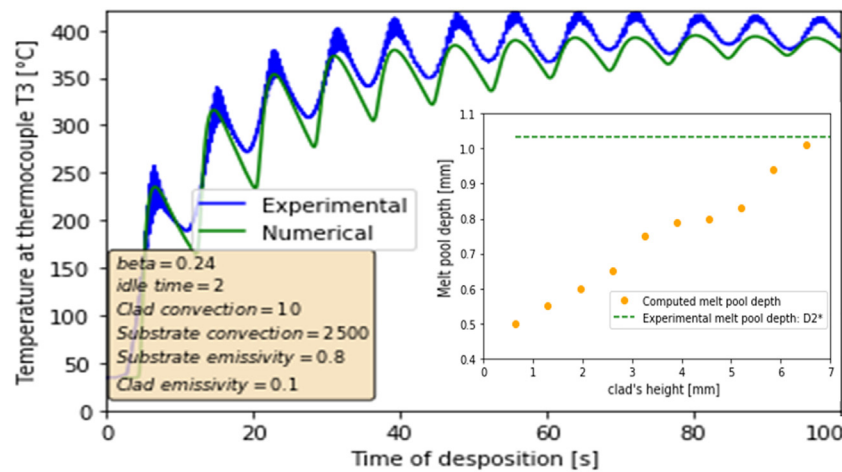**Fig. 15.** Sensitivity analysis: variation of emissivity ε (data set 2).

between the slope of the curve (Fig. 13) and not assuming an excessive impact of Marangoni effect.

5.1.2. Sensitivity to convection and radiation

To test the sensitivity of the model to convection and radiation parameters, two limit sets of values are chosen as illustrated in Table 3. In the first set, the convective heat transfer coefficient of the clad is varied from free convection (1–20 W/m²K) to relatively forced one (100–200 W/m²K), while emissivity is kept constant to 0.8 which is the approximate value for 316L SS [59]. In the second set, the clad convection is fixed (10 W/m²K) and values of emissivity vary from 1 (theoretical perfect emissivity) to a very low one (0.1). The values of β_{2D} and idle time are respectively kept 0.24 and 2 s. Large substrate sizes have a large heat extraction capacity allowing the material to substantially cool after each built layer, whereas small substrates favor heat build-up in the part [60]. As the 3*rd* dimension is ignored in 2D modeling, appropriate heat dissipation must be taken account in the model. Some numerical teams use substrate size as fitting parameter [27]. To avoid this practice which needs to modify the model dimensions and generate various meshes, a high convection value is defined as the boundary condition of the substrate. The chosen convection and radiation values for the substrate are respectively 2500 W/m²K and 0,8. These high levels of convection coefficients of both substrate subdivisions help to cool down the entire model and to maintain under control spurious numerical temperature oscillation. The h coefficient effect is shown, through temperature versus time curves at thermocouple T3, in Fig. 14. A difference of 40.3 °C is observed by the end of the deposition of the 10*th* layer demonstrating a sensitivity to the h variation. Note that the simulation has to run for ten layers to get the tendency. For a low number of layers, the impact is not accurate. Indeed, the height of the clad tends to increase with deposition time resulting in an increase of heat loss by convection and radiation. Between forced convection values (h = 100 or 200 W/m²K), no noticeable cooling is observed. When free convection is applied (values lower than 20 W/m²K), no impact of accurate data between 1 and 20 values is observed. As free convection gives result close to experimental curve, it will be used for studying the impact of radiation. According to simulation results in Fig. 15, an emissivity of 1 enhances an excessive cooling of the model compared to the experiment, while a quite low value of 0.1 gives a better trend of the numerical curve but is known not physical.

If the shape of the predicted curves as well as their numerical values seem to be close to the experimental curve, the predicted melt pool does
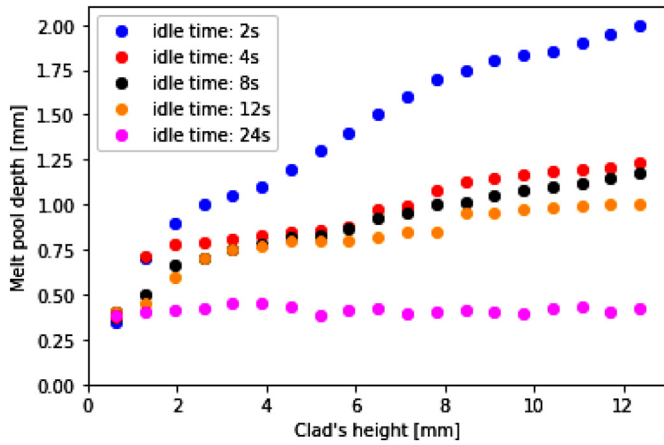

Fig. 16. Evolution of the predicted melt pool depth with a set of parameters giving a reasonnable prediction of temperature at T3.

Fig. 17. Sensitivity analysis: impact of the variation of idle time on melt pool depth.

Table 4
Optimized parameters ensuring the best compromise between melt pool evolution and thermocouple curve.

Parameter	Value				
β	0.355				
Idle time [s]	8				
h_{Clad} [W/m^{2}K]	Bloc 1	Bloc 2	Bloc 3	Bloc 4	Bloc 5
	500	50	80	150	170
ε_{Clad}	Bloc 1	Bloc 2	Bloc 3	Bloc 4	Bloc 5
	0.8	0.8	0.8	0.8	0.8

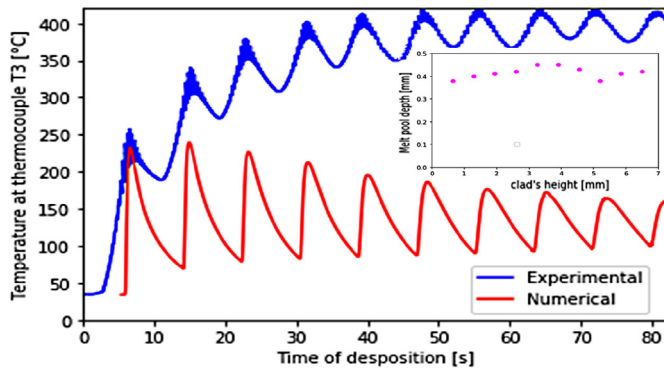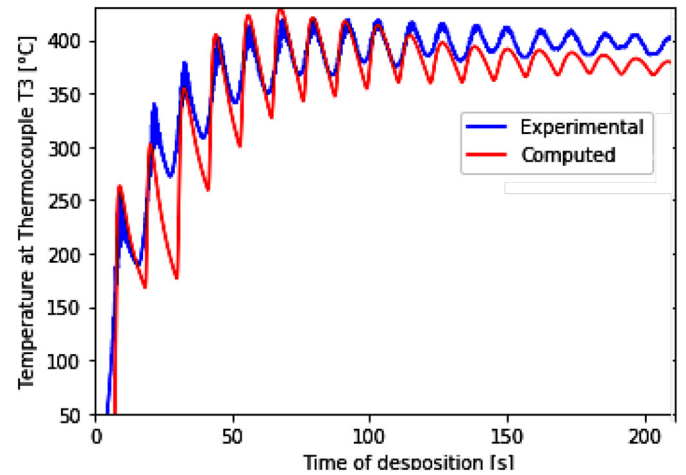**Fig. 20.** Experimental thermocouple curve versus numerical prediction.

Fig. 18. Disparity between temperature prediction and experiment when the set of parameters allow constant melt pool prediction.

not exhibit a constant evolution as shown in Fig. 16. So the model confirms the fact that low values of ε are indeed inconsistent. The predicted molten pool size tends to increase with deposition time which means that the heat input is not enough compensated by leaks through convection and radiation. The virtual idle time of 2 s is too short to let these leaks happen. The chosen laser power for the sets of simulations of Sections 5.1.1 and 5.1.2 is also not sufficient, which is clear by the fact that even the first layer is not completely molten (Fig. 13). So, β_{2D} should be more accurately defined.

5.1.3. Sensitivity to idle time

The increase of the virtual idle time allows to modify the slope of the melt pool depth-height curve (see Fig. 17). Chosen values of coefficients h and ε are respectively 10 W/m^{2}K and 1 for the clad. By rising the idle

time, the melt pool depth trend is more stable and a constant value is found for an idle time of 24 s. Note that β_{2D} was kept at its initial value within this sensitivity analysis but will be more accurately defined within the final identification step.

Although this idle time ensures a constant melt pool depth with deposition time, the associated numerical thermocouple curve is now not anymore in agreement with the experimental results as illustrated in Fig. 18. A good compromise is required between the different influential parameters on both thermocouple curve and melt pool depth. For idle time, the range from 4 to 12 s is of interest as it provides a better trend of the slope of the melt pool depth versus clad height curve.

5.2. Final identification of the model parameters

The methodology of the different simulations is shown in Fig. 19. In order to calibrate the model, the convection and radiation values are
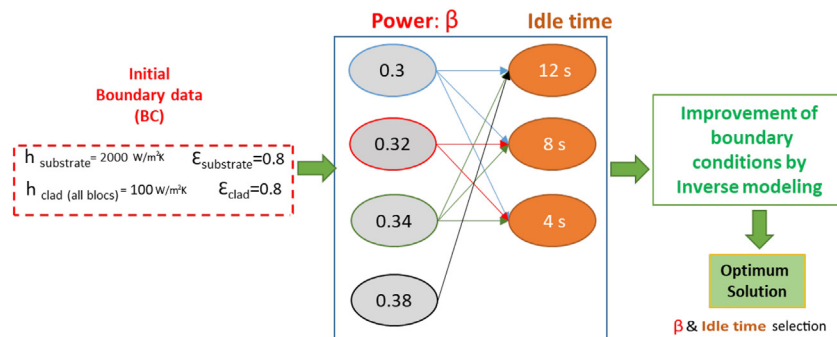

Fig. 19. Methodology of running simulations to obtain optimized set of parameters.
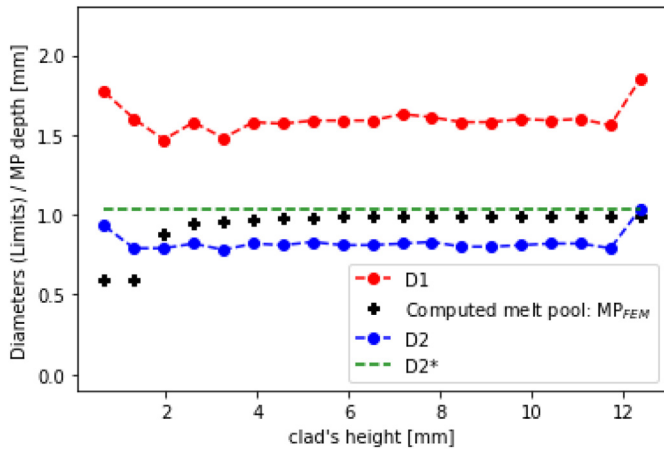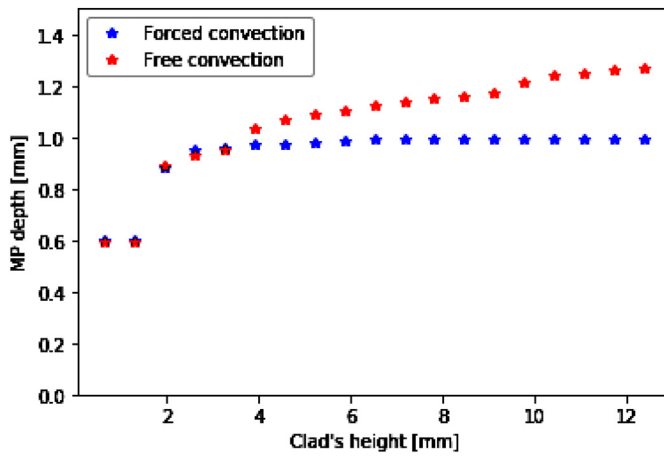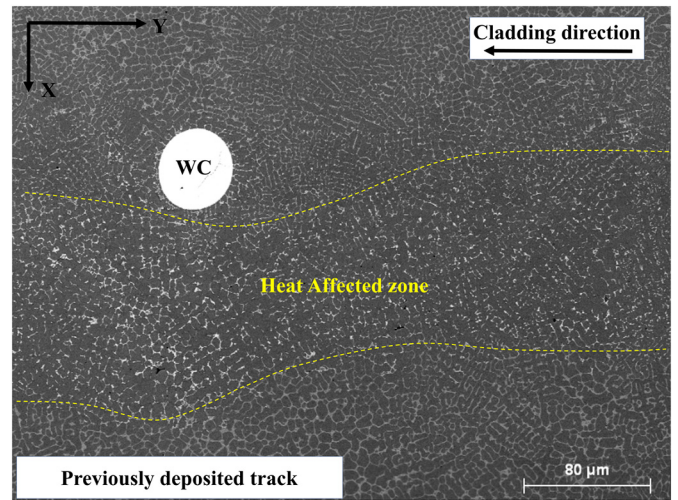
Fig. 21. Evolution of melt pool depth.

Fig. 24. SEM micrograph of the 316L + 20%WC microstructure at the 6*th* layer, showing a HAZ in between two tracks.

Fig. 22. Evolution of melt pool depth with clad height in case of free an forced convection of the clad.

first fixed to minimize the unknown parameters as the input data interface values have lower effect on the thermocouple curves than the laser power and idle time. In fact, laser power is step by step increased compared to the initial value of set in paragraph 5.1 and for each value, different idle times are tested. Optimum values of 0.3 for β_{2D} and 4 s for virtual idle time give acceptable results.

The final parameter identification is based on a fine tuning input of material parameters and boundary conditions by a successful prediction of both thermal history of T3 and melt pool depth. Studying the interval [8–12 s] of idle time results in an adequate loss of energy for the whole sample manufacturing. The final optimized parameters are gathered in Table 4.

Experimental thermocouple curve (scaled to the total simulation time, which represents the time required for deposition of middle layers to which is added the virtual idle periods) versus numerical prediction is shown in Fig. 20. The majority of the maximum peaks are well predicted by the numerical model. The effect of the increased virtual idle time (8 s against 2 s before calibration) is clear in the numerical curve.
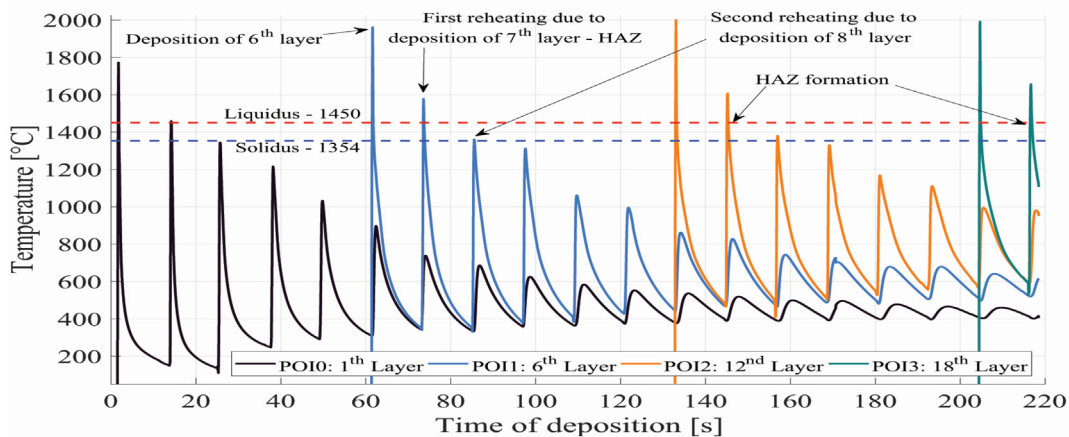

Fig. 23. Simulated thermal evolution of four POIs selected from three different zones within the deposit.

Table 5
Simulated thermal evolution of four POIs selected from three different zones within the deposit.

Point of Interest	Maximum peak temperature (°C)	Cooling Rate CR (°C/s)
0	1772.31	2256.11
1	1962.40	1945.10
2	2000.46	1696.31
3	2001.68	1654.62

Indeed, an excessive cooling after the first layers deposition results in minima lower than to the experimental curve. However, the minimum peaks become closer to experimental curve with increasing clad height due to heat accumulation during the process.

The predicted evolution of the melt pool depth is shown in Fig. 21. Starting from the 4th layer, the melt pool depth reaches the target

(a) Layer 6

(b) layer 12

(c) layer 18
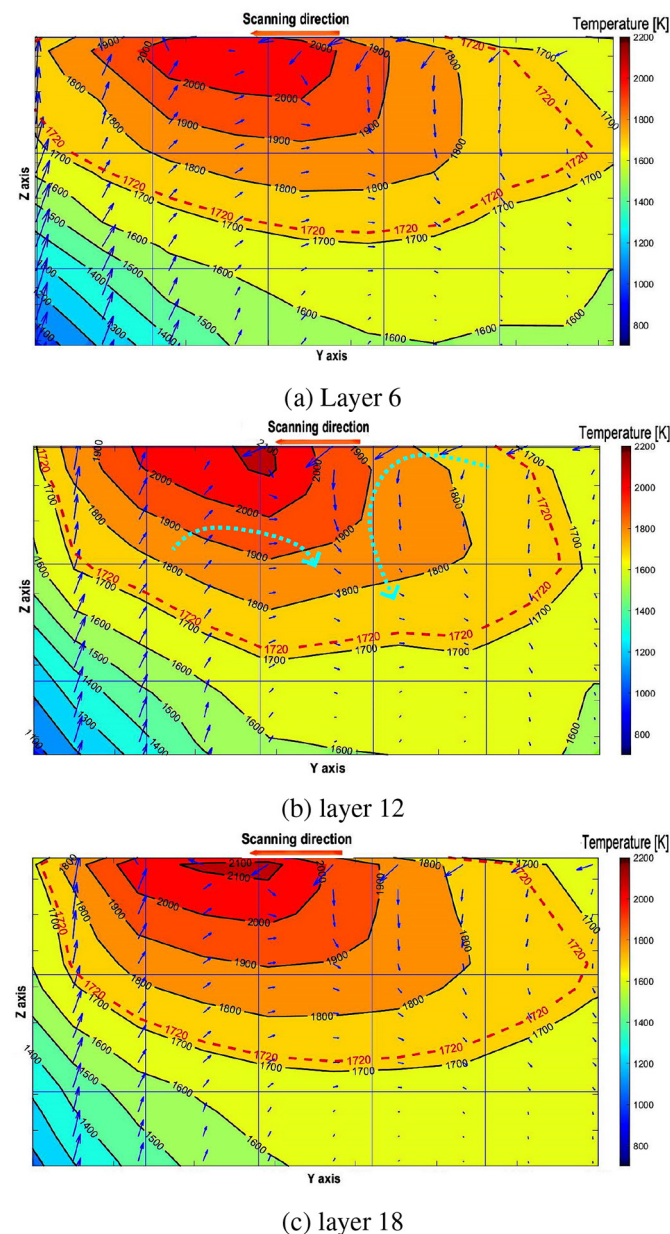
Fig. 25. Temperature distribution inside melt pools of the layers 6, 12 and 18. Thermal gradients are represented by arrows.

level of D_2^* and remains constant thorough the whole deposition time. However, predicting the correct depths of the first 3 layers is not obvious. Authors of this work are not the first researchers who found this type of discrepancy. In fact, Foroozmehr et al. [61] developed a 3-dimensional FEM model to predict thermal history as well as melt pool dimension during deposition of a single layer of 316L SS. They reported that melt pool reaches steady dimension after 3 tracks.

### 5.3. Importance of implementation of forced convection

Simulating the DED process with a free convection or a forced convection has an impact on the melt pool depth prediction as seen in Fig. 22. Here a value of h = 10 W/m$_2$K is affected to all layers for free convection case while forced convection values are those of the optimum solution. Forced convection assumption is a key point to correctly predict the melt pool depth which is associated with an accurate thermal gradient and cooling rate prediction during the DED process.

5.4. Heat accumulation and liquid phase analysis

For a better analysis of the thermal history during deposition, Fig. 23 considers thermal nodal points evolution computed for four different zones: the bottom (1st and 6th layers), medium (12th layer) and top (18th layer) parts of the clad. For each zone, a point of interest (POI) is defined. Each POI achieves solidus temperature (1354 °C) three times. The first and highest peak corresponds to the deposition of the considered layer. The second peak is related to the deposition of a further layer on the previously deposited one and the formation of a HAZ. As shown in Fig. 24, the HAZ of this composite is highlighted by the presence of $M_{23}C_6$ and M_6C solidification carbides while M_4C solidification carbides are observed in the track. Indeed, as shown in [11], the reheating due to the deposition of the next track or layer leads to the dissociation of the metastable M_4C carbides and thus a different local microstructure in the HAZ. The second reheating (Fig. 23) does not lead to further microstructural modifications. This infers that the actual solidus temperature during fabrication is at a higher level in comparison to the one set thought DTA test (1354 °C) since the low scan rates allow diffusion of elements [11].

For each POI, as computed in [62], the Cooling Rates (CR) are defined as the slopes between the peak temperature and the solidus. They decrease with clad height since, with the progress of the deposition, the heat accumulates in the deposit and decreases the temperature difference (noted ΔT) between the maximum peak temperature in the melt pool (hereafter noted $T_{max\ peak}$) and the already deposited material [22,25]. Indeed, at the beginning of the fabrication, the 316L substrate is at room temperature, which leads to the largest ΔT and the highest CR during the deposition (Table 5). With the progress of the deposition, the previously deposited layer is considered as an apparent substrate. Heat accumulation phenomenon is visible, especially when considering the minimum temperature reached after each peak zone, which shows a gradual increase throughout the deposition process. In addition, $T_{max\ peak}$ rises until a steady state is reached due to the increase in the heat loss at higher temperatures [22,57]. The decrease in ΔT and CR occurs even if the laser input energy is maintained constant during the whole deposition process. This is reported in literature [25,63].

The modification in the thermal conductivity within the melt pool (γ), used in this study, is a classical way to model the effect of fluid motion due to the thermo-capillary phenomenon. In particular, it exhibits a good representation of the effects of temperature rise. Indeed, the heat accumulation enhances the stirring of the melt pool due to Marangoni convection. Fig. 25 analyzes 3 melt pools (layers number 6, 12 and 18 respectively) to give a better visualization of the thermal gradient and molten flow. Dotted red lines indicate the liquidus boundaries when the temperature is above the liquidus of 1720 K (1450 °C). For the molten pool of each layer, the temperature field is similar: the maximum peak temperature is located around the middle of the top part of the
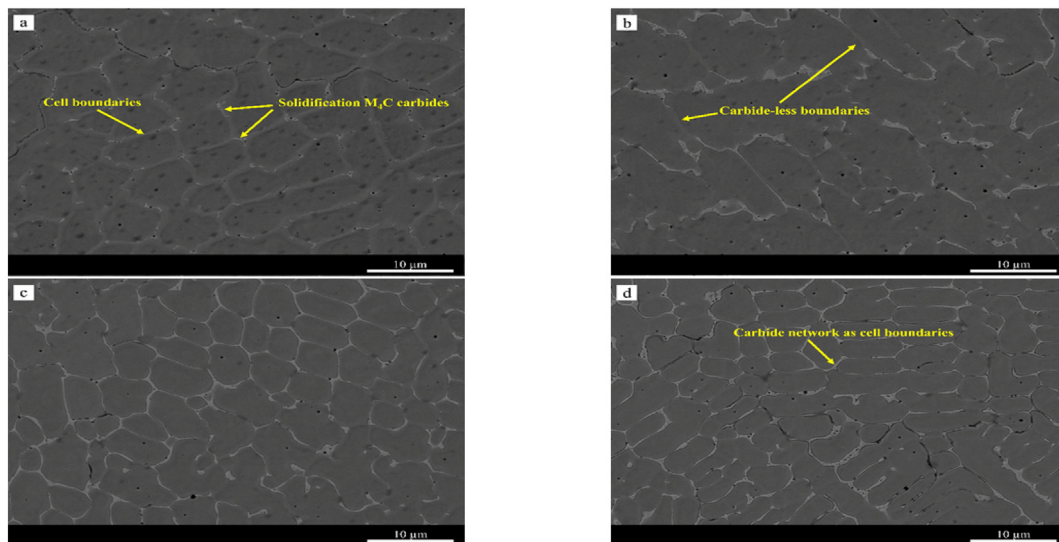
Fig. 26. SEM micrographs of the reinforced matrix at respectively (a) 1st layer, (b) 2nd-3rd layers, (c) 4th–5th layers and (d) 7th–8th layers, etched in aqua regia. (For interpretation of the references to colour in this figure legend, the reader is referred to the web version of this article.)

melt pool. Moreover, temperature values of the top part of the molten pool are remarkably higher than those of the bottom part. However, the distribution is not completely similar between the layers. This non-uniform distribution of temperature would be enhanced by liquid convective movements. It is reminded that mass flow is not considered in the model. In the real process, the surface tension gradients enhance rotational tendencies and generate fluid motion (Marangoni phenomenon). The FEM thermal model, using modified thermal conduction of the clad, increases conduction flow within the melt pool. The FE results suggest that a strong Marangoni flow exists as highly non-homogenous temperatures are predicted. The liquid mixing intensity would increase with rising height as maximum peak temperature increases and so the surface tension gradients.
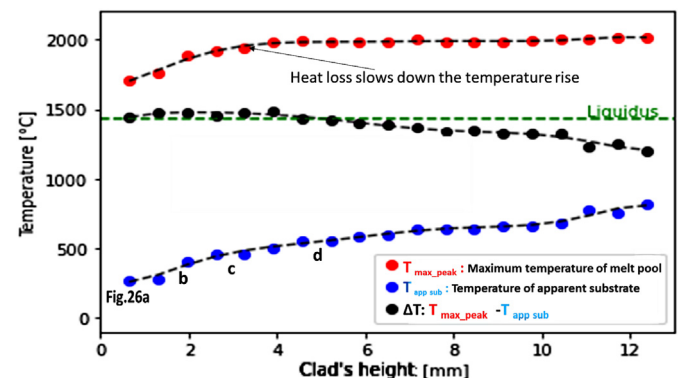
In addition to the local microstructure observed in the HAZ (Fig. 24), the tendencies of Fig. 23 and temperature fields highlighted in Fig. 25 lead to peculiar variation of the local microstructure in the layers. Indeed, four microstructures with different amount of solidification carbides can be distinguished (Fig. 26a to d) depending on the location. The formation of these microstructures depends on the thermal history and the Marangoni flows. Based on the thermal history shown in Fig. 23, in order to precisely estimate the temperature of the apparent substrate ($T_{app\ sub}$) and ΔT between this temperature and the maximum temperature reached by a given melt pool (the already defined $T_{max\ peak}$), the average value of 12 nodes (dotted area in Fig. 27) in front of the laser position was considered.
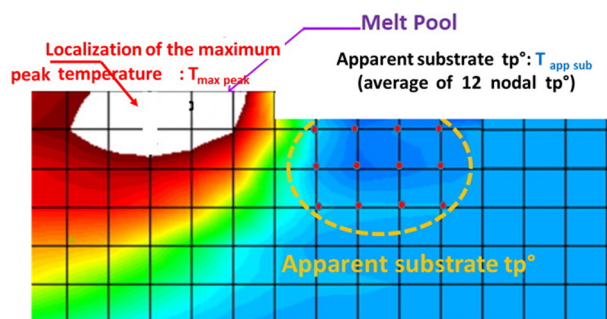
The evolutions of these 3 values are presented in the same plot in Fig. 28. As partially observed in Fig. 23, the trend of $T_{max\ peak}$ is a progressive increase during deposition, until reaching a steady level. It should be noted that the input energy allows reaching high temperatures already within the first tracks. $T_{max\ peak}$ rises from 1706 to 2017 °C by the end of the deposition. This continuous and slight increase is accompanied by a continuous and higher increase in the apparent substrate temperature. ΔT decreases along the sample height even though convection and radiation heat exchanges increase their magnitude from the bottom to the top (effect of both higher surface temperature and higher convection coefficient).

As shown Fig. 26a, the microstructure at the first layer exhibits the lowest amount of solidification carbides among the four positions due to the dilution of the composition since the first layer is deposited on the 316L substrate and due to the relatively highest CR (Table 5) in the fabrication [22,25,64]. The microstructure reminds more the cellular microstructure of a clad 316L with few solidification carbides at the cell boundaries [25]. Indeed, as shown in [11,65], the high temperatures of laser cladding lead to an initial stirring of the melt pool and especially the complete dissolution of the smaller WC particles at any given layer. This initial dissolution enriches the composition of the initial 316L in W and C, thus leading to solidification carbides after the formation of an austenitic matrix [11].

Fig. 27. Localization of the maximum temperature peak within the melt pool and apparent substrate temperature, average of substrate temperature values in front of the laser.

Fig. 28. Evolution of the maximum peak and apparent substrate temperatures as well as ΔT.

With the progress of the fabrication, the actual composition is attained since the deposition is carried out on previously deposited layers of the composite [64]. Furthermore, the Marangoni flows increase the stirring of the melt pool and the liquid lifetime increases since the CR decrease. In these conditions, the dissolution of the WC is enhanced and the composition is further enriched in W and C, thus increasing the amount of the solidification carbides. Indeed, as shown in Fig. 26b, at the 2nd and 3rd layers the quantity of carbide-less boundaries is decreased and the size of the solidification carbides is increased in comparison to Fig. 26a.

At the 4th and 5th layers, the further temperature rises (Fig. 28) and the increase of the melt pool stirring (Fig. 25) leads to a more homogenous reinforced microstructure with the formation of an almost continuous carbide network (Fig. 26c). When $T_{max\ peak}$ reaches a steady state close to 2000 °C (6th layer), the microstructure exhibits a continuous carbide network (Fig. 24 and Fig. 26d) without relevant modifications of the cellular microstructure up to the top of the deposit. With the temperature rise and the increase of the liquid lifetime, an increase of the dissolution cannot be excluded. Nevertheless, the carbide size and distribution are overall homogeneous in the whole height of the deposit (Figurs 5 and 6). On the other hand, as shown in [63,64,66], heat accumulation could lead to a coarsening of the microstructure with in particular, an increase of the grain size.

6. Conclusions

In this study, a thermal model was developed and is now ready to study the impact of process parameters. Even if fluid mechanics was not implemented in the FE model, the estimation of the level of the Marangoni effect was possible through the use of a modified conductivity. Furthermore, simplified assumptions of a 2D model were explained and an accurate identification methodology of the input parameters such as deposition time, numerical idle time and laser power was defined.

The numerical results are correlated with experimental observations that validate the model. It was found that the maximum peak temperature exhibits a slight increase during powder deposition to reach a steady value near 2000 °C. This value is below the melting point of WC carbides (~ 2750 °C), but allows their dissolution and, thanks to heat accumulation, the mixing of elements released by the carbide dissolution. After the computing of three layers, the melt pool depth remains constant (~1.03 mm) until the layer number 19 (last one), with the application of a constant applied laser power. This predicted result was mainly ensured by using a well tuned idle time and a variable forced convection magnitude allowing heat loss through boundaries and a correct equilibrium between input energy and boundary losses.

Such a 2D model indeed is of interest by offering quick prediction of the thermal history of the middle section of the clad during the process. These predicted data (thermal histories, remelting, cooling rates…) are useful, in particular in the case of a new material to understand microstructure generation. However, one limitation of such a model should be highlighted; the need of an additional experimentation to be applied on a new clad shape or a substrate geometry as it needs calibration.

It should be noted that the numerical output results were based on an experimental set that lead to various data, essentially through 4 thermocouples placed in different parts of the clad. Authors of this work plan to exploit available experimental data to carry out a comparison between 2D and 3D Finite Element modeling applied on the DED process of the investigated composite coating.

Declaration of Competing Interest

The authors declare that they have no known competing financial interests or personal relationships that could have appeared to influence the work reported in this paper.

Acknowledgements

References

[1] P. Liu, Z.W.Y.Z. Ji, C. Qiu, A. Antonysamy, L. Chen, L.C.X.Y. Cui, Investigation on evolution mechanisms of site-specific grain structures during metal additive manufacturing, J. Mater. Process. Technol. 257 (2018) 191–202.

[2] N. Hodge, R. Ferencz, J. Solberg, Implementation of a thermomechanical model for the simulation of selective laser melting, Comput. Mech. 54 (2014) 33–51.

[3] K. Zeng, D. Pal, H. Gong, N. Patil, B. Stucker, Comparison of 3DSIM thermal modelling of selective laser melting using new dynamic meshing method to ANSYS, Mater. Sci. Technol. 31 (2015) 945–956.

[4] W. Zhang, J. Turner, S. Babu, Building digital twins of 3D printing machines, Scr. Mater. 134 (2017) 61–65.

[5] Q. Portella, M. Chemkhi, D. Retraint, Influence of surface mechanical attrition treatment (SMAT) post-treatment on microstructural, mechanical and tensile behaviour of additive manufactured AISI 316L, Mater. Charact. 167 (2020) 110463.

[6] X. Wang, L. Zhao, J.Y.H. Fuh, H.P. Lee, Experimental characterization and micromechanical-statistical modeling of 316L stainless steel processed by selective laser melting, Comput. Mater. Sci. 177 (2020) 109595.

[7] E. Azinpour, R. Darabi, J. Cesar de Sa, A. Santos, J. Hodek, J. Dzugan, Fracture analysis in directed energy deposition (DED) manufactured 316L stainless steel using a phase-field approach, Finite Elem. Anal. Des. 177 (2020) 103417.

[8] G. Gray, V. Livescu, P. Rigg, C. Trujillo, C. Cady, S. Chen, J. Carpenter, T. Lienert, S. Fensin, Structure/property (constitutive and spallation response) of additively manufactured 316L stainless steel, Acta Mater. 138 (2017) 140–149.

[9] E. Ramirez-Cedillo, M.J. Uddin, J.A. Sandoval-Robles, R.A. Mirshams, L. Ruiz-Huerta, C.A. Rodriguez, H.R. Siller, Process planning of L-PBF of AISI 316L for improving surface quality and relating part integrity with microstructural characteristics, Surf. Coat. Technol. 396 (2020) 125956.

[10] S. Alvi, K. Saeidi, F. Akhtar, High temperature tribology and wear of selective laser melted (SLM) 316L stainless steel, Wear 448-449 (2020) 203228.

[11] T. Maurizi Enrici, O. Dedry, F. Boschini, J.T. Tchuindjang, A. Mertens, Microstructural and thermal characterization of 316L+WC composite coatings obtained by laser cladding, Adv. Eng. Mater. 22 (12) (2020) 2000291.

[12] D. Tanprayoon, S. Srisawadi, Y. Sato, M. Tsukamoto, T. Suga, Microstructure and hardness response of novel 316L stainless steel composite with TiN addition fabricated by SLM, Opt. Laser Technol. 129 (2020) 106238.

[13] D. Dai, D. Gu, Q. Ge, Y. Li, X. Shi, Y. Sun, S. Li, Mesoscopic study of thermal behavior, fluid dynamics and surface morphology during selective laser melting of Ti-based composites, Comput. Mater. Sci. 177 (2020) 109598.

[14] A. Mertens, T. L'Hoest, J. Magnien, R. Carrus, J. Lecomte-Beckers, On the elaboration of metal-ceramic composite coatings by laser cladding, THERMEC 2016, Vol. 879 of Materials Science Forum, Trans Tech Publications Ltd 2017, pp. 1288–1293.

[15] E. Toyserkani, A. Khajepour, S. Corbin, 3-D finite element modeling of laser cladding by powder injection: effects of laser pulse shaping on the process, Opt. Lasers Eng. 41 (20040) (2021) 849–867.

[16] C. Lalas, K. Tsirbas, K. Salonitis, G. Chryssolouris, An analytical model of the laser clad geometry, Int. J. Adv. Manuf. Technol. 32 (2007) 34–41.

[17] C. Baykasoğlu, O. Akyildiz, M. Tunay, A. C. To, A process-microstructure finite element simulation framework for predicting phase transformations and microhardness for directed energy deposition of Ti6Al4V, Addit. Manuf. 35 (2020) 101252.

[18] S. Santhanakrishnan, F. Kong, R. Kovacevic, An experimentally based thermo-kinetic hardening model for high power direct diode laser cladding, J. Mater. Process. Technol. 211 (2011) 1247–1259.

[19] C. Krill III, L.-Q. Chen, Computer simulation of 3-D grain growth using a phase-field model, Acta Mater. 50 (12) (2002) 3059–3075.

[20] L.-Q. Chen, Phase-field models for microstructure evolution, Annu. Rev. Mater. Res. 32 (2002) 113–140.

[21] Z. Zhang, P. Farahmand, R. Kovacevic, Laser cladding of 420 stainless steel with molybdenum on mild steel A36 by a high power direct diode laser, Mater. Des. 109 (2016) 686–699.

[22] G. Knapp, T. Mukherjee, J. Zuback, H. Wei, T. Palmer, A. De, T. DebRoy, Building blocks for a digital twin of additive manufacturing, Acta Mater. 135 (2017) 390–399.

[23] P. Prabhakar, W. Sames, R. Dehoff, S. Babu, Computational modeling of residual stress formation during the electron beam melting process for inconel 718, Addit. Manuf. 7 (2015) 83–91.

[24] L. Svensson, B. Gretoft, H. Bhadeshiay, An analysis of cooling curves from the fusion zone of steel weld deposits, Scand. J. Metall. 15 (1986).

[25] Y. Liu, J. Zhang, Z. Pang, Numerical and experimental investigation into the subsequent thermal cycling during selective laser melting of multi-layer 316L stainless steel, Opt. Laser Technol. 98 (2018) 23–32.

[26] R. Jardin, J.T. Tchuindjang, L. Duchêne, H.-S. Tran, N. Hashemi, R. Carrus, A. Mertens, A. Habraken, Thermal histories and microstructures in direct energy deposition of a high speed steel thick deposit, Mater. Lett. 236 (2019) 42–45.

[27] H. Yin, L. Wang, S.D. Felicelli, Comparison of two-dimensional and three-dimensional thermal models of the LENS® process, J. Heat Transf. 130 (10) (08 2008).

[28] W. Ya, B. Pathiraj, S. Liu, 2D modelling of clad geometry and resulting thermal cycles during laser cladding, J. Mater. Process. Technol. 230 (2016) 217–232.

[29] R. Parekh, R.K. Buddu, R. Patel, Multiphysics simulation of laser cladding process to study the effect of process parameters on clad geometry, Proced. Technol. 23 (2016) 529–536.

[30] F.A. España, V.K. Balla, A. Bandyopadhyay, Laser processing of bulk Al–12Si alloy: influence of microstructure on thermal properties, Philos. Mag. 91 (4) (2011) 574–588.

[31] W. Huang, Y. Zhang, Finite element simulation of thermal behavior in single-track multiple-layers thin wall without-support during selective laser melting, J. Manuf. Process. 42 (2019) 139–148.

[32] B. Khamidullin, I. Tsivilskiy, A. Gorunov, A. Gilmutdinov, Modeling of the effect of powder parameters on laser cladding using coaxial nozzle, Surf. Coat. Technol. 364 (2019) 430–443.

[33] V. Fallah, M. Alimardani, S.F. Corbin, A. Khajepour, Temporal development of melt-pool morphology and clad geometry in laser powder deposition, Comput. Mater. Sci. 50 (7) (2011) 2124–2134.

[34] M. Zheng, L. Wei, J. Chen, Q. Zhang, C. Zhong, X. Lin, W. Huang, A novel method for the molten pool and porosity formation modelling in selective laser melting, Int. J. Heat Mass Transf. 140 (2019) 1091–1105.

[35] A.J. Pinkerton, L. Li, The development of temperature fields and powder flow during laser direct metal deposition wall growth, Proc. Inst. Mech. Eng. C J. Mech. Eng. Sci. 218 (5) (2004) 531–541.

[36] A. Vasinonta, J.L. Beuth, M. Griffith, Process maps for predicting residual stress and melt pool size in the laser-based fabrication of thin-walled structures, J. Manuf. Sci. Eng. 129 (1) (2006) 101–109.

[37] L. Wang, S.D. Felicelli, P. Pratt, Residual stresses in LENS-deposited AISI 410 stainless steel plates, Mater. Sci. Eng. A 496 (1) (2008) 234–241.

[38] S. Kelly, S. Kampe, Microstructural evolution in laser-deposited multilayer Ti-6Al-4V builds: part ii. Thermal modeling, Mater. Sci. Eng. A 35 (2004) 1869–1879.

[39] R. Jendrzejewski, I. Kreja, G. Śliwiński, Temperature distribution in laser-clad multi-layers, Mater. Sci. Eng. A 379 (1) (2004) 313–320.

[40] M. Gouge, Chapter 3 - Convection boundary losses during laser cladding ** book, Thermo-Mechanical Modeling of Additive Manufacturing 2018, pp. 41–60.

[41] J. Heigel, P. Michaleris, E. Reutzel, Thermo-mechanical model development and validation of directed energy deposition additive manufacturing of Ti–6Al–4V, Addit. Manuf. 5 (2015) 9–19.

[42] S. Fetni, T. Maurizi Enrici, T. Niccolini, S.H. Tran, O. Dedry, R. Jardin, L. Duchêne, A. Mertens, A.M. Habraken, 2D thermal finite element analysis of laser cladding of 316L+WC composite coatings, Proced. Manuf. 50 (2020) 86–92 18th International Conference on Metal Forming 2020.

[43] L. Xin, M. Boutaous, S. Xin, D.A. Siginer, Numerical modeling of the heating phase of the selective laser sintering process, Int. J. Therm. Sci. 120 (2017) 50–62.

[44] A.C.A. Asséko, B. Cosson, M. Deleglise, F. Schmidt, Y.L. Maoult, E. Lafranche, Analytical and numerical modeling of light scattering in composite transmission laser welding process, Int. J. Mater. Form. 8 (2015) 127–135.

[45] C. Bonnet, F. Valiorgue, J. Rech, H. Hamdi, Improvement of the numerical modeling in orthogonal dry cutting of an AISI 316L stainless steel by the introduction of a new friction model, CIRP J. Manuf. Sci. Technol. 1 (2) (2008) 114–118 high Performance Cutting.

[46] K.S. Kumar, Numerical modeling and simulation of a butt joint welding of AISI 316L stainless steels using a pulsed laser beam, Mater. Today: Proceed. 2 (4) (2015) 2256–2266 4th International Conference on Materials Processing and Characterzation.

[47] O. Sayman, F. Sen, E. Celik, Y. Arman, Thermal stress analysis of WC–co/Cr–Ni multilayer coatings on 316L steel substrate during cooling process, Mater. Des. 30 (3) (2009) 770–774.

[48] W. Tang, X. Yang, S. Li, H. Li, Microstructure and properties of CLAM/316L steel friction stir welded joints, J. Mater. Process. Technol. 271 (2019) 189–201.

[49] P. Jiang, C. Wang, Q. Zhou, X. Shao, L. Shu, X. Li, Optimization of laser welding process parameters of stainless steel 316L using FEM, kriging and NSGA-II, Adv. Eng. Softw. 99 (2016) 147–160.

[50] L. Depradeux, Numerical Simulation of Welding-316L Steel Validation on Tests of Increasing Complexity, Ph.D. thesis, supervised by Jullien Jean-François Génie civil Lyon, INSA 2004, 2004.

[51] A. Mertens, S. Reginster, H. Paydas, Q. Contrepois, T. Dormal, O. Lemaire, J. Lecomte-Beckers, Mechanical properties of alloy Ti–6Al–4V and of stainless steel 316L processed by selective laser melting: influence of out-of-equilibrium microstructures, Powder Metall. 57 (3) (2014) 184–189.

[52] V. Tuninetti, G. Gilles, O. Milis, T. Pardoen, A. Habraken, Anisotropy and tension–compression asymmetry modeling of the room temperature plastic response of Ti–6Alâ–4V, Int. J. Plast. 67 (2015) 53–68.

[53] J.I.V. de Sena, C.F. Guzman, L. Duchene, A.M. Habraken, R.A.F. Valente, R.J.A. de Sousa, Numerical simulation of a conical shape made by single point incremental, AIP Conf. Proceed. 1567 (2013) 852.

[54] M. Chiumenti, M. Cervera, A. Salmi, C.A. de Saracibar, N. Dialami, K. Matsui, Finite element modeling of multi-pass welding and shaped metal deposition processes, Comput. Methods Appl. Mech. Eng. 199 (37) (2010) 2343–2359.

[55] T. Niccolini, Thermal Simulation on 316L + 20% vol WC Composite Sample Produced by Laser Cladding Additive Process, Master's thesis University of Liège - Faculty of Applied Sciences, 2020, URL http://hdl.handle.net/2268.2/9144.

[56] R. Brusten, Laser Cladding Finite Element Modelling. Application to Ti–6Al–4V, Master's thesis University of Liège - Faculty of Applied Sciences, 2015 , URL http://hdl.handle.net/2268.2/2390.

[57] V. Manvatkar, A. De, T. DebRoy, Heat transfer and material flow during laser assisted multi-layer additive manufacturing, J. Appl. Phys. 116 (2014).

[58] A. Kumar, C. Paul, A. Pathak, P. Bhargava, L. Kukreja, A finer modeling approach for numerically predicting single track geometry in two dimensions during laser rapid manufacturing, Opt. Laser Technol. 44 (3) (2012) 555–565.

[59] F. Valiorgue, A. Brosse, P. Naisson, J. Rech, H. Hamdi, J.M. Bergheau, Emissivity calibration for temperatures measurement using thermography in the context of machining, Appl. Therm. Eng. 58 (1) (2013) 321–326.

[60] L. Costa, R. Vilar, T. Reti, A. Deus, Rapid tooling by laser powder deposition: process simulation using finite element analysis, Acta Mater. 53 (14) (2005) 3987–3999.

[61] A. Foroozmehr, M. Badrossamay, E. Foroozmehr, S. Golabi, Finite element simulation of selective laser melting process considering optical penetration depth of laser in powder bed, Mater. Des. 89 (2016) 255–263.

[62] H.-S. Tran, J. Tchuindjang, H. Paydas, A. Mertens, R. Jardin, L. Duchêne, R. Carrus, J. Lecomte-Beckers, A. Habraken, 3D thermal finite element analysis of laser cladding processed Ti-6Al-4V part with microstructural correlations, Mater. Des. 128 (2017) 130–142.

[63] J. Zuback, T. DebRoy, The hardness of additively manufactured alloys, Materials (Basel) 11 (2018).

[64] O. Ertugrul, T. Maurizi Enrici, H. Paydas, E. Saggionetto, F. Boschini, A. Mertens, Laser cladding of tic reinforced 316l stainless steel composites: feedstock powder preparation and microstructural evaluation, Powder Technol. 375 (2020) 384–396.

[65] X. Tong, F. Hai Li, M. Kuang, W. You Ma, X. Chi Chen, M. Liu, Effects of wc particle size on the wear resistance of laser surface alloyed medium carbon steel, Appl. Surf. Sci. 258 (7) (2012) 3214–3220.

[66] Z. Xia, J. Xu, J. Shi, T. Shi, C. Sun, D. Qiu, Microstructure evolution and mechanical properties of reduced activation steel manufactured through laser directed energy deposition, Addit. Manuf. 33 (2020) 101114.